

Resolving the ionized wind of the post-Red Supergiant IRC +10 420 with VLTI/AMBER[★]

W.J. de Wit¹, R.D. Oudmaijer¹, M.A.T. Groenewegen², M.G. Hoare¹, and F. Malbet³

¹ School of Physics & Astronomy, University of Leeds, Woodhouse Lane, Leeds LS2 9JT, UK

² Institute for Astronomy, University of Leuven, Celestijnenlaan 200D, 3001 Leuven, Belgium

³ Laboratoire d'Astrophysique, Observatoire de Grenoble, BP 53, 38041 Grenoble, Cédex 9, France

Received date; accepted date

ABSTRACT

Aims. The paper investigates the milli-arcsecond scale structure of the present-day mass-loss of the post-Red Supergiant IRC +10 420 .

Methods. We use three telescopes of the VLT Interferometer in combination with the AMBER near-infrared beam combiner to measure spectrally dispersed correlated fluxes in the *K*-band around the Bry transition. The resulting visibilities are compared to the predicted visibilities of emission structures with various simple models in order to infer the size of the observed emission region.

Results. The Bry line is resolved by VLTI+AMBER on all three baselines, with the maximum projected baseline extending 69 meter and a P.A. ranging between 10° and 30°. A differential phase between line and continuum is detected on the longest baseline. The Bry emission region is found to have a diameter of 3.3 milli-arcseconds (FWHM), when compared to a Gaussian intensity distribution. A uniform disk and a ring-like intensity distribution do not fit the line visibilities. The size of the continuum emission is not constrained by the observations. Comparing the AMBER equivalent width of Bry with measurements from various epochs, we find that the stellar photosphere contributes about 60% of the total continuum light at 2.2 μ m. The remaining 40% continuum emission is found on scales larger than the 66 mas AMBER field of view. This independently confirms similar results made by previous studies. If the Bry emission is optically thin, then the observations do not allow to make any inferences about the shape of the line forming region. However, there is indirect evidence that the hydrogen recombination line emission is optically thick. In that case, using simple arguments, we find that the line emitting region is elongated. This is because the spectrum indicates that the projected line emitting area is about twice that of the stellar surface. This value is an order of magnitude less than a circular Bry line emitting area would have using the measured size of the emission region along our baseline. We briefly discuss the possibilities whether such a structure is due to a bi-polar flow or a circumstellar disk.

Key words. stars: evolution - stars: mass loss - supergiants - stars:individual IRC +10 420 - techniques: interferometric

1. Introduction

Throughout the evolution of a high-mass star, stellar winds carry off a significant fraction of the initial star mass. This process dominates their evolution and determines their final fate. In the late stages of massive star evolution, important information of the mass loss process due to stellar winds is contained in the complicated circumstellar nebulae, like the ones found near e.g. LBVs and Wolf-Rayet stars (Nota et al. 1995; Nota & Clampin 1997; Van der Sluys & Lamers 2003). The nebulae may disclose the mass-loss history, identifying phases with varying stellar wind properties like the wind momentum, geometry and total mass lost. One explanation for the observed nebula geometry is that the different mass loss episodes lead to wind-wind interactions, in the sense that a more re-

cent fast wind collides with a pre-existing slower expanding wind. Crucially, at least one of these winds should be asymmetric, possibly induced by mass loss anisotropies at the stellar surface (Maeder 2002). During which evolutionary phase this would actually occur is not known however, and various ideas have been put forward (see e.g. Mellema 1997; Heger & Langer 1998; Dwarkadas & Owocki 2002).

IRC +10420 is one of the few stars that evolve from the Red Supergiant (RSG) phase back towards the blue, witnessed by an extremely rapid increase in its surface temperature of ~ 2200 K over an interval of 30 years currently having a mid-A spectral type (see Oudmaijer et al. 1996; Klochkova et al. 2002). Its estimated distance of 3.5 to 5 kpc implies a luminosity typical for a star with an initial mass of around $40 M_{\odot}$, putting it close to the Humphreys-Davidson limit in the Hertzsprung-Russell diagram (Jones et al. 1993). The star is bright at 2.2 μ m ($K_s = 3.6$) and exhibits a huge infrared excess due to warm dust indicating that it was only recently in

Send offprint requests to: W.J. de Wit, e-mail: w.j.m.dewit@leeds.ac.uk

[★] Based on observations with VLTI, proposal 077.D-0388

an extreme mass-losing Red Supergiant phase (Oudmaijer et al. 1996). These properties make the star a prime candidate to eventually become a Wolf-Rayet star, surrounded by an intricate nebula (Jones et al. 1993)

The circumstellar environment of IRC +10 420 has various distinctive components. We list the basic features on the various size scales. Based on HST imaging, IRC +10 420's optical reflection nebula portrays a spherical distribution on scales larger than $2''$ out to 6 to $8''$ (Humphreys et al. 1997). Sphericity of the circumstellar material on this scale is seen at other wavelengths too, e.g. in the J -band by Kastner & Weintraub (1995), and in CO transitions by Castro-Carrizo et al. (2007). On a scale of about $1''$, one finds a bipolar geometry, with two patches of K -band and mid-IR emission to the NE and SW direction of the star (Humphreys et al. 1997). Given the relatively large distance from the central star, this emission should be scattered radiation. The location of these patches corresponds to an approximate position angle of 40° . Closer in and down to $0.3''$, HST reveals a complicated and non-uniform distribution of various jet-like, ray and arc features (Humphreys et al. 1997).

At even smaller angular scales, the dusty environment giving rise to the near-IR excess has been resolved with speckle interferometry at $2.11\mu\text{m}$ (Blöcker et al. 1999). Modelling the spectral energy distribution (SED) and visibility curves with DUSTY leads these authors to conclude that IRC +10 420 is surrounded by two separate spherical shells with diameters of $0.070''$ and $0.310''$ centred on the star. Finally, the geometry on a size scale comparable to the stellar radius (\sim milliarcseconds) can be probed with the various emission lines, like $H\alpha$ and Fe II , that are reflected off the large scale blue nebula (Humphreys et al. 2002; Davies et al. 2007). With IFU observations of the nebula, Davies et al. find evidence for a present-day wind which has an axi-symmetric, rather than spherically symmetric geometry. The $H\alpha$ emission symmetry axis is found to have a position angle of 33° .

In this paper on IRC +10 420 we present complementary observations of the subarcsecond ionised and continuum emitting material inside the 70 mas dust shell found by Blöcker et al. (1999). These authors found that about 60% of the K -band continuum emission remains unresolved (see also Monnier et al. 2004), presumably corresponding to the star itself. We use the VLT interferometer in conjunction with the near-IR three telescope beam combiner AMBER, attaining a maximum spatial resolution of 6.5 mas. The ultimate objective is to measure the size and shape of the $\text{Br}\gamma$ emission line region, giving a direct measurement of the present-day mass-loss geometry, an important ingredient to the mass-loss puzzle. In Sect. 2 we present the AMBER data, and provide a list of steps and considerations taken in the reduction process. Results regarding the final visibility, flux and differential phase spectra of IRC +10 420 are presented in Sect. 3. In this section we derive the size for the continuum and $\text{Br}\gamma$ emission. We discuss the shape of the $\text{Br}\gamma$ emission region in Sect. 4. The latter is found to be elongated along the VLTI baseline of the observation with a P.A. of $\sim 20^\circ$. We conclude our findings in Sect. 5.

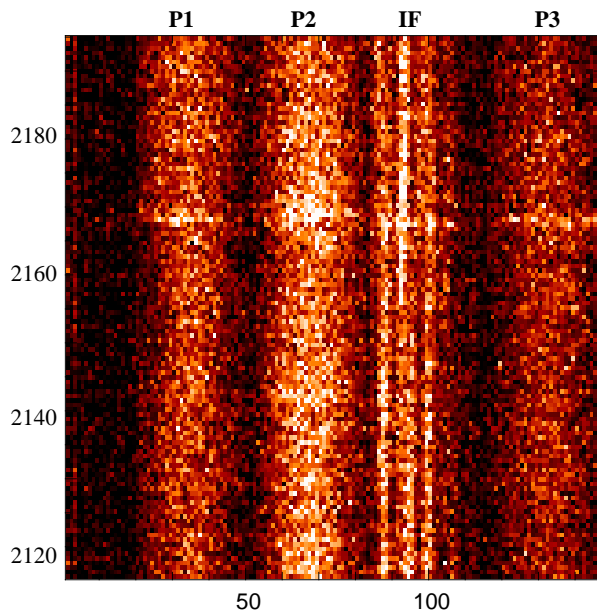


Fig. 1. Illustration of an AMBER frame of the target star IRC +10 420 showing fringes. An approximate wavelength scale in nm is given along the y-axis, pixels along x-axis. The frame gives the three telescope channels (P1, P2, P3), and the interferometric channel (IF). The $\text{Br}\gamma$ emission line can be identified as the horizontal enhancement in recorded ADUs.

2. Observations and data reduction

2.1. AMBER data reduction: general considerations

AMBER is the VLTI's near infrared, three telescope beam combiner (Petrov et al. 2007). The interferometric beam is fed into a spectrograph delivering a spectrally dispersed interferogram that is spatially encoded on a detector. AMBER can operate with two or three telescopes, and offers three spectral resolutions. The AMBER data reduction is not (yet) a straightforward process and particular care should be taken in reducing and analysing the data.

The reduction of AMBER data can be split in two distinctive steps. Ever since the discovery of an electronic interference pattern on the detector (Li Causi et al. 2008), a first reduction step must involve a digital filtering process that needs to be applied to all data taken with AMBER. A software routine by the name of AMDC has been developed that identifies the electronic interference frequencies in Fourier space by means of a dark frame, and creates a "Fourier mask". This mask needs to be applied to the data, and AMDC replaces the power at the corrupted frequencies with a new value based on the power at the neighbouring frequencies.

The second step consists of converting the Fourier filtered AMBER data to (raw) visibilities. This step can be done using the dedicated AMBER software *amdlib* written by the consortium (see Tatulli et al. 2007 for an in depth explanation). In short, the software algorithm relies on a mathematical description of the interferogram, with empirical input from the calibration and alignment unit of the AMBER instrument. It records VLTI+AMBER instrumental characteristics at the be-

Table 1. Predicted and measured continuum visibilities for IRC +10 420 and the calibrator star HR 7648. IRC +10 420 has an observed upper limit to its diameter of 3 mas (Monnier et al. 2004), whereas the calibrator has a uniform disk diameter of 1.95 mas (Richichi et al. 2005). Corresponding theoretical visibilities are given in cols.(2) and (6). The measured raw values of V_{cont}^2 in cols. (3) and (7) correspond to the average continuum value for a SNR frame selection of 20% (see text), these values are subject to systematic uncertainties. The uncertainties on the raw V_{cont}^2 given reflect the internal variation. Col.(8) is the calibrated V_{cont}^2 . Col. (9) gives the ratio between the line and continuum (see Fig. 3). Col. (10) is the range for V_{Bry} as derived in Sect. 3.3, taking into account the various uncertainty contributions.

	HR7648			IRC +10 420						
	Baseline (m) (1)	V_{UD} theo. (2)	$\langle V_{\text{cont}}^2 \rangle$ raw (3)	Baseline (m) (4)	P.A. ° (5)	V theo. (6)	$\langle V_{\text{cont}}^2 \rangle$ raw (7)	$\langle V_{\text{cont}}^2 \rangle$ calib. (8)	$V_{\text{cont}}^2/V_{\text{Bry}}^2$ (9)	V_{Bry} (10)
U1-U2	43.9	0.96	0.111 ± 0.002	39.8	12.8	> 0.92	0.169 ± 0.004	1.46 ± 0.03	1.36 ± 0.07	0.60–0.74
U2-U3	35.8	0.97	0.149 ± 0.003	30.3	32.7	> 0.95	0.210 ± 0.005	1.37 ± 0.03	1.20 ± 0.07	0.74–0.89
U3-U1	78.7	0.87	0.201 ± 0.004	69.1	21.5	> 0.76	0.265 ± 0.005	1.15 ± 0.03	1.68 ± 0.06	0.39–0.57

gining of each night, and they are used to create the so-called pixel-to-visibility matrix (P2VM). The P2VM converts subsequently the observed science target fringe patterns into a measurement of coherent flux. Alongside the contemporaneous registration of the total photometric flux spectrum at each telescope for each interferogram recorded, the data reduction package calculates the interferometry observables, i.e. in case of three telescopes, the three squared visibilities, closure phase, and differential phase. An example of an AMBER frame of IRC +10 420 is given in Fig. 1. It consists of three telescope channels and an interferometric channel. In this figure an approximate wavelength scale is given on the vertical axis (no wavelength calibration has been applied). The presence of Bry emission is identified by the bright horizontal line, crossing the three photometric and interferometric channels.

2.2. Observations with AMBER

VLTI+AMBER observed IRC +10 420 on the nights of 14th and 15th June 2006. The observations were performed in the UT1-UT2-UT3 baseline configuration. UT4 was not available during these nights due to technical problems. The telescope configuration delivers projected baselines between ~ 40 and ~ 70 meters and a limited P.A. coverage of about 20° (see Table 1). The AMBER instrument was set-up in the medium spectral resolution mode, delivering a spectral resolution of 1500. This chosen wavelength range lies between 2.12 and $2.19\mu\text{m}$, and includes the Bry transition. Bry has been reported to be in emission by Oudmaijer et al. (1994) and the size of the emitting region is the goal of our AMBER observations of IRC +10 420.

On the first night a total of 15 observations of IRC +10 420 was secured over a period of one hour under reasonable weather conditions. On the second night 5 observations were secured under bad weather conditions. Each observation with AMBER produces a file that consists of 1000 individual exposures, called frames. Each frame is then made up of the individual photometric information for each telescope aperture and the interferometric beam information (the interferogram), all as function of wavelength (see Fig. 1). The integration time

per frame was chosen to be 50 ms. The integration time is limited by the movement of the fringes over the detector by atmospheric turbulence (the so-called jitter), causing attenuation of the fringe visibility.

In order to perform an absolute calibration of the AMBER visibilities, an interferometric calibrator star was observed 5 times each night. The calibrator star is catalogued as HR 7648 (SAO 125355). It is a $K = 2.2$, K5 III star with a uniform disk diameter of 1.95 ± 0.02 mas derived from spectrophotometric data (Richichi et al. 2005). The ASPRO tool¹ returns a size of 2.056 ± 0.142 mas for HR 7648 based on magnitude-colour calibration (like V vs $V - K$) of angular diameters. The calibrator's size is thus not directly measured using interferometry. The object was chosen as it is close on the sky to IRC +10 420 and it is expected to remain (nearly) unresolved (see Table 1). Note, that the calibrator is considerably brighter than the expected correlated magnitude of the science target (60% of $K = 3.6$, Monnier et al. 2004). The calibrator was observed 5 consecutive times, one hour after the first IRC +10 420 observation, with the same exposure time as the target. The observation of the calibration star was done under worse seeing ($1.1'' - 1.2''$) conditions than the target star ($0.8''$), which implies better AO correction during the target observations.

All AMBER data were corrected for electronic interference noise using the AMDC software by Li Causi et al. (2007), and reduced using *amdl*ib (versions 1.21 and 2.0 beta) software with frame bin size 1, i.e. no averaging over the 1000 frames present in each file. The additional data reduction files, namely a bad pixel map and a flatfield were taken from the AMBER website (versions of 9 Feb 2006) and used in the reduction process. Visual inspection using the ammyorick environment (see e.g. Millour et al. 2007) shows that only the first five IRC +10 420 observations do actually contain frames with fringes.

A measure of successfully interfering the three telescope beams and recording of fringes is given by the *amdl*ib package parameter signal-to-noise ratio (SNR). The expression for this parameter can be found in eq. (20) of Tatulli et al. (2007a). It is

¹ ASPRO is a java applet for the preparation and simulation of VLTI observations; see http://www.mariotti.fr/aspro_page.htm.

based on the weighted summing of the correlated flux over all spectral channels per interferogram. There is a strong need to apply a data quality (fringe quality) check to AMBER data due to non-stationary vibrations in the interferometer infrastructure, which for the moment are uncontrollable. The currently recommended approach regarding these data quality degrading effects is by making a frame selection based on the SNR criterion, and subsequently disregarding low SNR frames up to a certain cut-off (e.g. see Tatulli et al. 2007b). The SNR values calculated by *amdlib* for these observations range between 1 and 4. The other ten observations of the first night suffer from very low fluxes, hardly rising above the detector noise level. The five calibrator observations are all of relatively good quality, with some frame SNR values reaching 10. Observations of the second night are also of low quality. The results presented in this paper are therefore based on the first five observations of both IRC +10 420 and HR 7648 taken during the first night.

Practical experience has led to the compromise to choosing the best 20% of the frames during the frame selection process (Tatulli et al. 2007a). This 20% SNR cut-off was chosen only by the consistent AMBER visibility results it has provided (see e.g. Malbet et al. 2007). In our case the 20% selection for calibrator and target would lead to unphysical calibrated target continuum visibilities larger than one ($\langle V_{\text{cal}}^2 \rangle$ in Table 1). However, we shall show in the next subsection that frame selection does not seriously affect the *relative* AMBER visibilities.

The current quality of AMBER data limits the ability to perform an absolute calibration of the continuum visibilities. Instead, we will use the results from previous high-angular resolution studies in the literature. We quote in Table 1 an upper limit to the diameter of IRC +10 420's continuum emitting region of 3 mas based on Keck Interferometer observations in the *K*-band (Monnier et al. 2004). We have listed the corresponding visibility lower limits for a uniform disk for each VLTI baseline. We note that 3 mas is probably a generous size upper limit for the continuum emitting region, if it corresponds to the underlying star only. A simple calculation shows that for a luminosity of IRC +10 420 of $25\,462\text{ (d/kpc)}^2 L_{\odot}$ (Blöcker et al. 1999) and a mid A spectral type (Oudmaijer et al. 1996), a much smaller stellar diameter of ~ 0.70 mas can be expected. This result is independent of distance. If instead the stellar disk of IRC +10 420 were equal to the ~ 3 mas upper limit, then its spectral type would consequently need to be M-type, which is inconsistent with IRC +10 420's A-type spectrum. As we shall argue below, other contributions to the continuum as seen by AMBER by dust or any bound-free/free-free emission is small.

3. Results

3.1. AMBER flux, visibility, and phase spectra

The panels of Fig. 2 show the extracted AMBER observables for each UT baseline: the flux (top), visibility (middle) and the differential phase (bottom) spectra. The flux spectra are normalised to one (at Bry). No explicit wavelength calibration has been performed, and the spectra have simply been shifted in wavelength in order to match the emission line with the Bry rest wavelength. The spectra have been divided by the inter-

ferometric calibrator star in order to remove telluric absorption components. The flux spectra show the Bry transition clearly in emission, as has been reported by three other papers previously (Oudmaijer et al. 1994; Hanson et al. 1996; Humphreys et al. 2002), with spectra taken in 1992, 1994, and 2000 respectively. The line has an equivalent width (EW) of -7Å , which is significantly stronger than found in the above mentioned studies. We discuss this difference in the next subsection.

The second row of three panels present the visibility spectra. The spectra are the average of 20% best SNR frames. Following the discussion on the calibration of the continuum visibilities, we have set its value to one, i.e. a spatially unresolved continuum (see also next subsection). The important result of these observations is however the smaller visibility in the Bry emission line as function of baseline. We note that the shortest baseline is the U2-U3 baseline, where the deviation from a spatially unresolved Bry line is smallest.

Crucial for the relative visibility at the Bry line with respect to the continuum is its stability as function of the frame selection criteria. To test this, we apply a SNR frame selection with an increasing percentage of frames selected and for each selection we calculate the relative visibility of the Bry line. We start with a minimum percentage of 20% and increase it with steps of 20%. For each selection we measure the average of the continuum (excluding the Bry transition). The minimum in the Bry transition is taken to be the minimum of a Gaussian profile fit to the resulting visibility spectrum. The evolution of the fraction $V_{\text{cont}}^2/V_{\text{Bry}}^2$ as function of percentage of selected frames is shown in Fig. 3. The figure shows that this fraction slightly increases with the percentage of frames selected. A bias towards smaller values of V^2 is introduced when selecting more frames explains the observed trend. This is because a correct estimate of V^2 requires a certain level for the incoming flux. With Bry in emission, more line flux is available for beam combination than in the adjacent continuum. A reasonable estimate for V_{Bry}^2 exists therefore for a larger fraction of the frames than for the V_{cont}^2 estimate. Increasing the number of selected frames will thus bias the V_{Bry}^2 less than it does V_{cont}^2 , resulting in a larger value for their ratio. The errorbars on the measurements in Fig. 2 are representative of the variance of the continuum visibility level, averaged over the indicated number of selected frames. The figure shows that the strongest relative dependence on frame selection is found for the shortest baseline 2 (U2-U3), where Bry has the smallest deviation from the continuum. The relative visibility changes at most with 0.1 for this baseline. The variation of these fractions are taken into account in the uncertainty in the ratio between line and continuum as quoted in Table 1. We thus conclude that the AMBER relative visibilities of IRC +10 420 are stable within the uncertainties listed.

Finally, the last row of panels in Fig. 2 shows the differential phase for each baseline. The differential phase is an approximate measure for the spatial offset of the photocentre on the projected baseline at a certain wavelength relative to some reference wavelength. The data show no change in differential phase over the Bry line on the first two baselines (but perhaps a trace is present on the second baseline). A phase change of 5 to 10 degrees in the Bry line with respect to the continuum

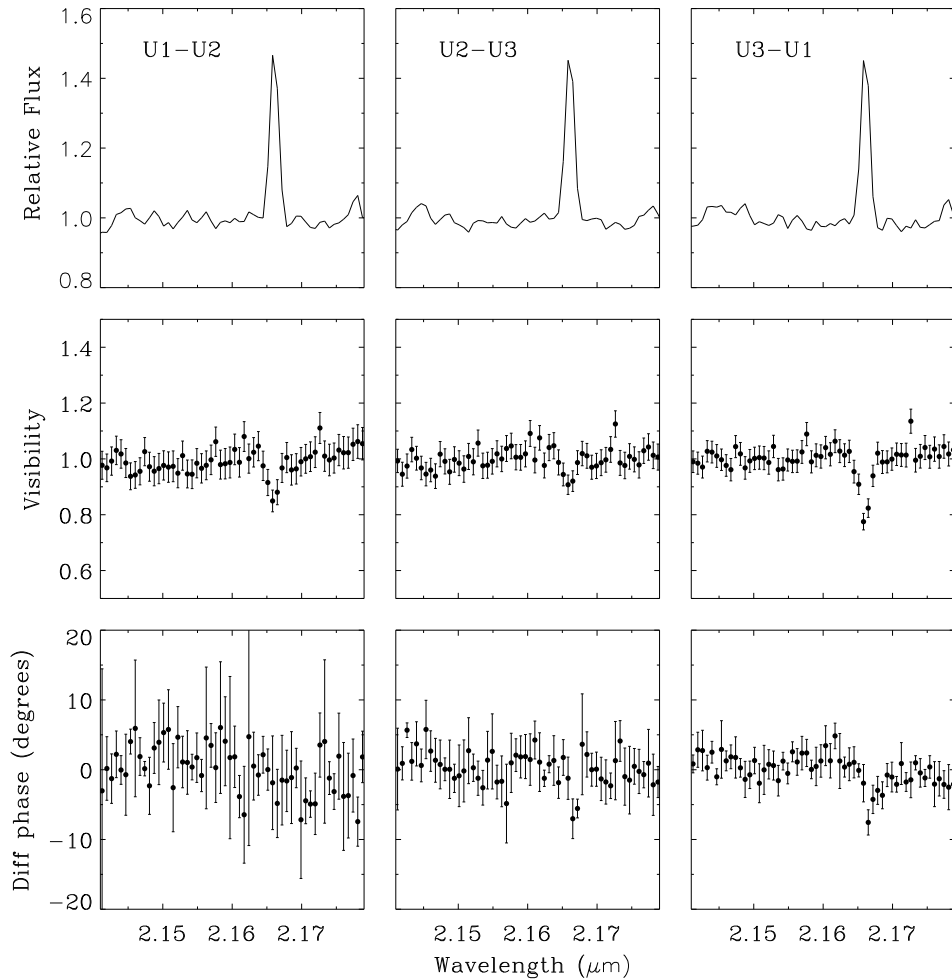


Fig. 2. AMBER flux (top), visibility (middle) and differential phase (bottom) spectra of IRC +10 420 for each of the three VLTI U1-U2-U3 configurations. The flux spectrum is divided by a telluric standard and normalized to one. The continuum visibility is normalised to a value of one near Br γ (see discussion in text). The Br γ emission line has a smaller visibility than the continuum at all three baselines. A phase change is detected for the U3-U1 baseline.

is detected on the third baseline. This constitutes an offset of the Br γ photocentre of about 0.1 mas, and will be discussed in Sect. 3.3.

The fourth AMBER observable, the closure phase, shows a random white noise scatter with an rms of 25° around 0° (for 20% best SNR frame selection), without any trace of a signal around the Br γ transition.

3.2. Size scales of the dusty CS environment

The total K -band emission of IRC +10 420 appears to consist of almost equal contributions by the photosphere and the hot CS dust (Oudmaijer et al. 1996). They find a good SED fit for a star surrounded by two dust shells at distances larger than 86 stellar radii (30 mas). The Blöcker et al. (1999) interferometric observations resolve $\sim 40\%$ of the K -band emission, and subsequent modelling of both the SED and visibilities reveals two dust shells with a minimum radius ~ 35 mas (see also

Sect. 1). The 60% flux component remains unresolved even for baselines up to 36 meters as probed with IOTA (Monnier et al. 2004). Evidently, most of the K -band excess corresponds to this dust component, leaving at most 10% of the *total* continuum due to another source. This could be either dust or gas emission located much closer to the star and unresolved by IOTA. The relatively large $\text{EW}(\text{Br}\gamma) = -7\text{\AA}$ found from the AMBER flux spectra is consistent with the idea of a 40% reduction of the K -band continuum due to a field of view effect rather than variability in the amount of Br γ flux. Previous observations reported $\text{EW}(\text{Br}\gamma)$ of -1.2\AA (Oudmaijer et al. 1994) and -4\AA (Humphreys et al. 2002). The question is how much the Br γ emission has varied between the 2000 spectrum by Humphreys et al. and the AMBER spectrum of 2006. An as yet unpublished spectrum taken by our group at the NTT with the SOFI imaging spectrograph in 2005, has an $\text{EW}(\text{Br}\gamma)$ of -4.5\AA , i.e. hardly any change with respect to 2000. This is in line with $\text{EW}(H\alpha)$ that varied relatively little over that same pe-

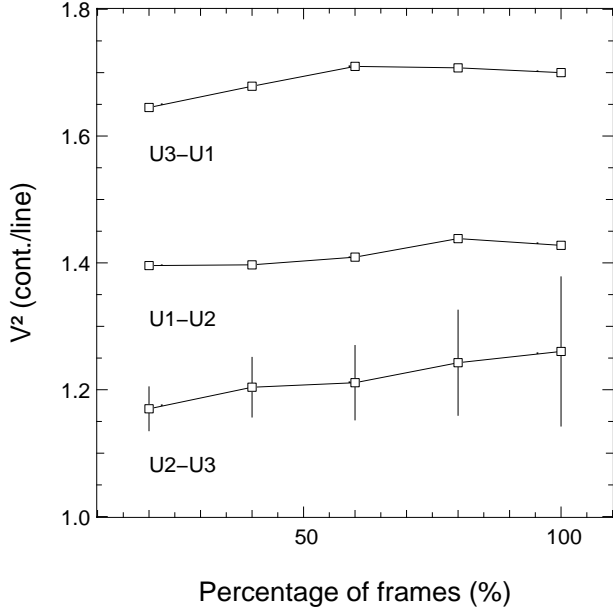


Fig. 3. The ratio of the continuum squared visibility to the Br γ squared visibility as function of the number of frames selected. The errorbars indicate the continuum variance per spectrum averaged over the selected frames. For clarity purposes, the errorbars are plotted for one baseline only.

riod (Patel et al. 2008). Assuming thus no change in Br γ emission, we conclude that $\sim 40\%$ less continuum must have been observed in the AMBER data, which indicates that most dust is outside AMBER’s field of view (66 mas).

3.3. Size scale of the Br γ emission region

The size of the Br γ emitting region can be derived from the line visibilities. We estimate the visibility of the Br γ emission component by applying the definition for the total visibility of a multi-component source :

$$V_{\text{Br}\gamma+\text{cont}} = \frac{V_{\text{cont}} \times F_{\text{cont}} + V_{\text{Br}\gamma} \times F_{\text{Br}\gamma}}{F_{\text{cont}} + F_{\text{Br}\gamma}}. \quad (1)$$

We solve for $V_{\text{Br}\gamma}$ using the observed line and continuum flux ratios from the spectrum. However in this procedure there are uncertainties involved regarding the absolute level of V_{cont} as previously discussed and the value of F_{cont} . F_{cont} is uncertain in the sense that at Br γ the proper underlying photospheric absorption profile has to be used. We recall that the ratio of V_{cont} to $V_{\text{Br}\gamma+\text{cont}}$ is stable as shown in Sect. 3.1, V_{cont} however could in principle lie between the values corresponding to the 3mas upper limit from IOTA, or be fully unresolved.

Eq. (1) is valid if there does not exist a differential phase between line and continuum (see e.g. Weigelt et al. 2007). The effect of the detected U3-U1 differential phase on the line visibility is marginal compared to other uncertainties that we will discuss next.

First, we estimate the value for F_{cont} in eq. (1) that needs to correspond to the photospheric absorption feature. We estimate the absorption feature from the spectral type of IRC +10 420 , viz. mid A-type. We introduce into the AMBER spectrum a

Gaussian absorption profile with EWs of 5 and 6Å with a FWHM similar to the emission line. This EW is about the average for A-type Ia supergiants as reported in Hanson et al. (1996). The ratio of $F_{\text{Br}\gamma}$ to the adjacent continuum is 1.48, whereas the ratio of $F_{\text{Br}\gamma}$ to the minimum flux level of the photospheric absorption profile is between 1.97 and 2.08 for an equivalent width of 5Å and 6Å respectively. Given the discussed uncertainties in the continuum visibilities, we derive a range of values for the Br γ visibility at each baseline. The derived values are presented in Fig. 4 and listed in Table 1.

In the figure we fit the Br γ visibilities to three simple geometrical light distributions, viz. the uniform disk, the Gaussian distribution, and a ring distribution. The uncertainty is dominated by three factors, (1) uncertainty of the absolute calibration of the continuum visibility, between 3 mas and unresolved, (2) uncertainty of the relative strength of Br γ visibilities relative to the continuum (see Table 1 col. (9)), and (3) uncertainty regarding the underlying photospheric absorption. All these three uncertainties are taken into account in the range of Br γ visibilities plotted in Fig. 4 and listed in col. (10) in Table 1. The figure clearly demonstrates that the shapes of the visibility curves as function of baseline do not follow the observed visibilities in case of a uniform disk and a ring. On the other hand the Gaussian distribution can reproduce the observations, albeit marginally. The Gaussian distribution of Fig. 4 has a FWHM of 3.3 mas. We thus conclude that the Br γ emitting region on the sky of IRC +10 420 takes the shape of a Gaussian-like distribution with a FWHM of ~ 12 AU ($d = 3.5$ kpc), at least between the measured baseline position angles, i.e. between a P.A. of $\sim 10^\circ$ and $\sim 30^\circ$.

4. Discussion: Geometry of the Br γ emission region

The shape of the emitting region can not be further constrained by the visibility measurements alone, given the limited P.A. range of our VLTI observations. Only when the line is optically thick can we infer a geometry by means of the total Br γ flux and the total continuum flux for an equivalent wavelength range (taken to be the full width of the emission line). Indeed, in that case, the flux will be approximated by $F_L = B_\nu(\nu, T)\Delta\nu\left(\frac{R}{d}\right)^2$ (cf. Oudmaijer et al. 1994; see also Grundstrom & Gies 2006), with B_ν the Planck function, $\Delta\nu$ the linewidth, unresolved in our data but measured to have a FWHM of 64 kms $^{-1}$ by Oudmaijer et al. (1994) and only slightly broader in Humphreys et al. (2002), R represents the radius of the emitting surface if it is circular, and d is the distance. The line optical depth has no bearing on the size of the Br γ emitting region as determined in the previous section.

Oudmaijer et al. (1994) present the dereddened linefluxes of several optical and near-infrared hydrogen recombination lines and demonstrate that the line ratios deviate significantly from case B. For example, IRC +10 420 shows $F_{\text{Br}\gamma} \sim F_{\text{Br}\alpha}$, a line ratio that indicates that Br α is optically thick (case B predicts a ratio of 0.33). This would not necessarily imply that Br γ is optically thick of course, but we note that the models by Simon et al. (1983) indicate that Br γ is almost as strong as Br α

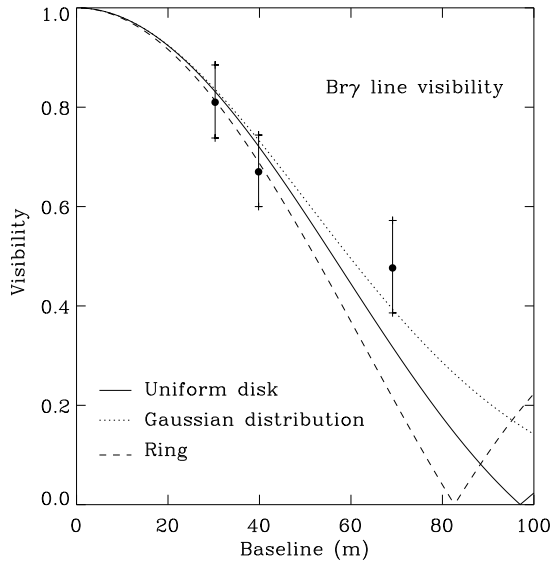


Fig. 4. The final visibilities of the Bry emitting region. The range in values is determined by the uncertainty in photospheric absorption, the absolute continuum visibility, and the error on the relative visibility of the line. Three simple, symmetric models have been fit to the data. The Gaussian model fits with a FWHM of 3.3 mas.

for a very large range of optical depths for both Bry and Br α . As both H α and the Bry line have become stronger over the years (see Patel et al. 2007 and above respectively), we conclude that it is reasonable to assume the line to be optically thick.

Inspection of the above equation immediately indicates that we can directly compare the size of the emitting region with that of the star, emitting at the same wavelength by taking the ratio

$$\left(\frac{F_L}{F_*}\right) = \left(\frac{B_\nu(\nu, T_L) A_L}{B_\nu(\nu, T_*) A_*}\right) \quad (2)$$

With T_L , T_* , A_L , A_* , the temperature and the projected surface area of the line emitting region and the star respectively. In the AMBER data, taking into account filling in of the photospheric absorption profile by the line emission, we find that the emission lineflux $F_L \sim F_*$. Assuming a stellar temperature of 8500 K and a temperature of the ionized region of 5000 K, we can then use Eq. 2 to compute the ratio of line emitting surface area and the stellar disk, which turns out to be 1.7. If we take the same temperature for the star as for the line emitting region, we find a lower limit to the ratio of 1. So, the flux spectrum indicates that an optically thick line emitting area would be less than twice the size of the stellar photosphere.

How does this compare with the results from the AMBER interferometry? We recall that the Gaussian fit to the visibility of the resolved Bry line gave a FWHM for the Bry line emitting area at our projected baseline of 3.3 mas. This diameter is 5 times larger than the stellar diameter as derived from spectral energy distribution considerations and even larger than the

upper limit of 3 mas found by Monnier et al. Hence, if the optically thick Bry came from a circular region on the sky, then based on the observed and inferred size scales of the line emitting region and the star respectively, we would predict the line flux to be at least an order of magnitude larger than is actually observed. This apparent contradiction between observed and expected line fluxes can most straightforwardly be explained if the line emitting surface is not circular, but has an asymmetric, elongated, appearance, with the measured size scale along the major axis.

Such an apparent disparity is not unusual, and is a well documented property of Be stars. Their, optically thick, H α lines are known to originate from a disk and the line fluxes are also comparable to the continuum flux, implying small emitting areas. However, in the case where the emission is resolved, the disks' major axes are much larger than the unresolved stars. Indeed, the effect is so general that the H α EW can be used to estimate the extension of the disks (see e.g. Grundstrom & Gies 2006).

In summary, the Bry line visibilities indicate that AMBER resolves the line emitting region, and we derive a corresponding size of $5 R_*$. The region produces a much larger line-to-continuum flux ratio than observed in the AMBER flux spectrum, under the assumption of optically thick emission. From this discrepancy one may infer that the Bry emitting region is actually elongated on the sky along the North-Eastern direction, with a P.A. of about 20° . A caveat is of course that for an optically thin Bry line no such conclusions can be made regarding the geometry of the emitting region.

That the circumstellar material of IRC +10 420 exhibits a North-Eastern extension at larger scales than probed here may not be a coincidence. The outer reflection nebula in the HST images of Humphreys et al. (1997) is elongated along a PA of 33° , while Davies, Oudmaijer & Sahu (2007) find from a study of the reflected optical spectrum off the dust, that the H α emission has an axis of symmetry aligned with the extended reflection nebula. Although their data do not allow any conclusions to be drawn about whether the H α emission is elongated along or perpendicular to the long axis of the dusty reflection nebula.

The open question is what the nature of the wind is, is the ionized material located in a bi-polar flow type of geometry or in an edge-on disk? Pending velocity resolved high resolution imaging of the recombination lines, we restrict ourselves to the following. The only velocity information known about the large shell around the object is ambiguous. On the one hand Nedoluha & Bowers (1992) find from their high resolution imaging in the OH masers that the Northern part is tilted toward the observer and the Southern part moves away. This picture would favour a bi-polar geometry, as the velocity difference between the northern and southern components is too large to be realistically explained by Keplerian motions. On the other hand, Castro-Carrizo et al. (2007) find in their sub-arcsecond imaging of the CO rotational line emission a largely symmetric appearance, but, intriguingly, present a southern component approaching the observer, opposite to Nedoluha & Bowers data. Clearly, the nature of even the large scale structure of the circumstellar data is not settled yet.

5. Conclusions

We have presented VLTI/AMBER observations in the *K*-band of the post-Red Supergiant transition object IRC +10 420, with the aim to spatially resolve the $\text{Br}\gamma$ emission region. The observations were done with three UT telescopes and consist of intermediate spectral resolution spectra of the coherent and incoherent flux of IRC +10 420 within the AMBER field of view of 66 mas and with an angular resolution of 6.5 mas. The telescope configuration probed a range of 20° in position angle. The conclusions of this study are as follows.

- The AMBER visibility spectra show a decreased $\text{Br}\gamma$ line visibility for all three baselines. It indicates that the line emitting region has been resolved. The continuum visibilities on the other hand are not constrained by this dataset. We fit the $\text{Br}\gamma$ line visibilities with simple intensity distributions, and find that a Gaussian distribution with a FWHM of 3.3 mas fits the data best. The derived diameter corresponds to a distance of approximately $5 R_*$ from the central star.
- The AMBER differential phase spectra show a change in phase for the U3-U1 baseline at the $\text{Br}\gamma$ transition. This could indicate an offset of the photocentre projected on this baseline. New measurements of better quality would help to characterize the nature of this signal.
- The AMBER flux spectra show the $\text{Br}\gamma$ line of IRC +10 420 in emission. It is stronger than reported by two previous studies. We have argued that this is due to the fact that most of the *K*-band excess emission is located outside the AMBER field of view. This result is consistent with the speckle-interferometric results presented previously by Blöcker et al. (1999), where they find the inner most dust sphere to have a diameter of 70 mas.

We have speculated on the geometry of the $\text{Br}\gamma$ emitting region, concluding that it would be elongated along the interferometer baseline if the emission is optically thick. Optically thick emission seems however to be consistent with observed line ratios. Additional measurements perpendicular to the baselines presented here will help in further constraining the processes that shape the environment of this massive star in transition to its final fate.

Acknowledgements. We would like to thank Ben Davies for useful discussions, and Andrew Clarke for communicating his results on the near-infrared spectrum. This manuscript benefited from insightful comments by an anonymous referee.

References

Blöcker, T., Balega, Y., Hofmann, K.-H., et al. 1999, *A&A*, 348, 805
 Castro-Carrizo, A., Quintana-Lacaci, G., Bujarrabal, V., Neri, R., & Alcolea, J. 2007, *A&A*, 465, 457
 Davies, B., Oudmaijer, R. D., & Sahu, K. C. 2007, *ApJ*, 671, 2059
 Dwarkadas, V. V. & Owocki, S. P. 2002, *ApJ*, 581, 1337

Grundstrom, E. D. & Gies, D. R. 2006, *ApJ*, 651, L53
 Hanson, M. M., Conti, P. S., & Rieke, M. J. 1996, *ApJS*, 107, 281
 Heger, A. & Langer, N. 1998, *A&A*, 334, 210
 Humphreys, R. M., Davidson, K., & Smith, N. 2002, *AJ*, 124, 1026
 Humphreys, R. M., Smith, N., Davidson, K., et al. 1997, *AJ*, 114, 2778
 Jones, T. J., Humphreys, R. M., Gehrz, R. D., et al. 1993, *ApJ*, 411, 323
 Kastner, J. H. & Weintraub, D. A. 1995, *ApJ*, 452, 833
 Klochkova, V. G., Yushkin, M. V., Chentsov, E. L., & Panchuk, V. E. 2002, *Astronomy Reports*, 46, 139
 Li Causi, G.L., et al., 2008, *A&A* subm.
 Maeder, A. 2002, *A&A*, 392, 575
 Malbet, F., Benisty, M., de Wit, W.-J., et al. 2007, *A&A*, 464, 43
 Mellema, G. 1997, *A&A*, 321, L29
 Millour, F., Petrov, R., Malbet, F., et al. 2007, *ArXiv e-prints*, 705
 Monnier, J. D., Millan-Gabet, R., Tuthill, P. G., et al. 2004, *ApJ*, 605, 436
 Nedoluha, G. E. & Bowers, P. F. 1992, *ApJ*, 392, 249
 Nota, A. & Clampin, M. 1997, in *Astronomical Society of the Pacific Conference Series*, Vol. 120, *Luminous Blue Variables: Massive Stars in Transition*, ed. A. Nota & H. Lamers, 303
 Nota, A., Livio, M., Clampin, M., & Schulte-Ladbeck, R. 1995, *ApJ*, 448, 788
 Oudmaijer, R. D., Geballe, T. R., Waters, L. B. F. M., & Sahu, K. C. 1994, *A&A*, 281, L33
 Oudmaijer, R. D., Groenewegen, M. A. T., Matthews, H. E., Blommaert, J. A. D. L., & Sahu, K. C. 1996, *MNRAS*, 280, 1062
 Patel, M., Oudmaijer, R. D., Vink, J.S., 2008, *MNRAS*, subm.
 Petrov, R. G., Malbet, F., Weigelt, G., et al. 2007, *A&A*, 464, 1
 Richichi, A., Percheron, I., & Khristoforova, M. 2005, *A&A*, 431, 773
 Simon, M., Felli, M., Massi, M., Cassar, L., & Fischer, J. 1983, *ApJ*, 266, 623
 Tatulli, E., Isella, A., Natta, A., et al. 2007, *A&A*, 464, 55
 Tatulli, E., Millour, F., Chelli, A., et al. 2007, *A&A*, 464, 29
 van der Sluys, M. V. & Lamers, H. J. G. L. M. 2003, *A&A*, 398, 181

List of Objects

‘HR 7648’ on page 3